

RESEARCH ARTICLE | SEPTEMBER 29 2022

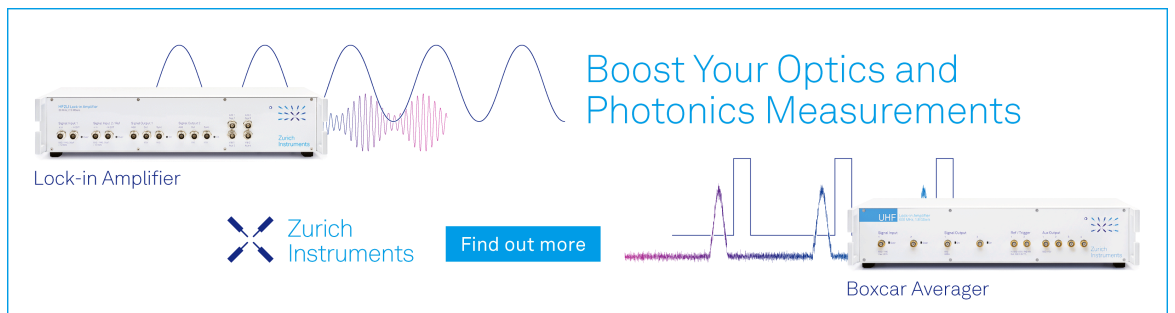
Fiber-tip endoscope for optical and microwave control

Stefan Dix; Jonas Gutsche; Erik Waller; Georg von Freymann ; Artur Widera  




Rev. Sci. Instrum. 93, 095104 (2022)

<https://doi.org/10.1063/5.0100330>



Boost Your Optics and Photonics Measurements

Lock-in Amplifier

 [Find out more](#)

Boxcar Averager

Fiber-tip endoscope for optical and microwave control

Cite as: Rev. Sci. Instrum. 93, 095104 (2022); doi: 10.1063/5.0100330

Submitted: 23 May 2022 • Accepted: 27 August 2022 •

Published Online: 29 September 2022 • Publisher Error Corrected: 03 October 2022



View Online



Export Citation



CrossMark

Stefan Dix,¹ Jonas Gutsche,¹ Erik Waller,^{1,2} Georg von Freyemann,^{1,2}  and Artur Widera^{1,a)} 

AFFILIATIONS

¹Department of Physics and State Research Center OPTIMAS, University of Kaiserslautern, Erwin-Schroedinger-Str. 46, 67663 Kaiserslautern, Germany

²Fraunhofer Institute for Industrial Mathematics ITWM, Fraunhofer-Platz 1, 67663 Kaiserslautern, Germany

^{a)}Author to whom correspondence should be addressed: widera@physik.uni-kl.de

ABSTRACT

We present a robust, fiber-based endoscope with a silver direct-laser-written structure for radio frequency (RF) emission next to the optical fiber facet. Thereby, we are able to excite and probe a sample, such as nitrogen-vacancy (NV) centers in diamond, with RF and optical signals simultaneously and specifically measure the fluorescence of the sample fully through the fiber. At our targeted frequency range of around 2.9 GHz, the facet of the fiber core is in the near-field of the RF-guiding silver structure, which comes with the advantage of an optimal RF intensity decreasing rapidly with the distance. By creating a silver structure on the cladding of the optical fiber, we achieve the minimal possible distance between an optically excited and detected sample and an antenna structure without affecting the optical performance of the fiber. This allows us to realize a high RF amplitude at the sample's position when considering an endoscope solution with integrated optical and RF access. The capabilities of the endoscope are quantified by optically detected magnetic resonance (ODMR) measurements of an NV-doped microdiamond that we probe as a practical use case. We demonstrate a magnetic sensitivity of our device of $17.8 \text{ nT}/\sqrt{\text{Hz}}$ when measuring the ODMR exclusively through our fiber and compare the sensitivity to a measurement using a confocal microscope. Moreover, the application of our device is not limited to NV centers in diamonds. Similar endoscope-like devices combining optical excitation and detection with radio frequency or microwave antenna could be used as a powerful tool for measuring a variety of fluorescent particles that have so far only been investigated with bulky and large optical setups. Furthermore, our endoscope points toward precise distance measurements based on Rabi oscillations.

© 2022 Author(s). All article content, except where otherwise noted, is licensed under a Creative Commons Attribution (CC BY) license (<http://creativecommons.org/licenses/by/4.0/>). <https://doi.org/10.1063/5.0100330>

I. INTRODUCTION

During the last two decades, the nitrogen-vacancy (NV) center in diamond has been extensively studied for magnetic field sensing^{1,2} and thermometry in bio-medical applications³ as well as quantum information processing.⁴ As a sensor, this solid-state system can be addressed, manipulated, and read out harnessing optical and microwave (MW) fields⁵ and reaches sensitivities in the order of $\eta < 1 \text{ nT}/\sqrt{\text{Hz}}$.⁶ Furthermore, it has been observed in host crystals as small as 5 nm^{7,8} and has been introduced into living cells.³ This extreme miniaturization and compatibility goes well beyond the capabilities of, e.g., alkali vapor cells,⁹ which have been shown to exhibit even improved sensitivities of $\eta < 1 \text{ fT}/\sqrt{\text{Hz}}$.^{10,11}

Usually, solid-state color centers are investigated optically in a microscope with an additional microwave setup.¹² Therefore, a variety of fiber-tip integrations have been developed relaxing the need for bulky measurement apparatus. However, in most of these applications, the microwave fields, which are crucial for spin-manipulation, were supplied by an external antenna located at a comparatively large distance in the order of a few millimeters to the host diamond.^{13–19} In order to reduce the overall MW powers applied to an examined sample in close proximity, which are typically in the range from mW to several W,²⁰ and to simultaneously sustain the driving field strength needed for vector magnetometry with NV centers, a coupling of the magnetic near-field component to the spins is necessary. Here, we present the prototype of a fiber-tip antenna that allows MW manipulation as well as optical control

of NV centers simultaneously. A schematic drawing and two images of the fabricated device are shown in Fig. 1. It consists of a commercially available multimode fiber and two attached silver wires which are fixed in position with epoxy resin. The wires are connected by an Ω -shaped antenna fabricated using metallic direct laser writing (mDLW) in a silver-based photo-resist on the fiber facet²¹ and conductivity is increased in a galvanic post process. Such antennas are widely applied for magnetometry with NV centers due to their homogeneous magnetic field in the center.²² The diameter of the prototype has a size of $d = 2.5$ mm in order to use commercially available tools for fiber processing and to fit into fiber caps for storage. We emphasize that the diameter can be further reduced without changing the general production steps. The length of the prototype's fiber is $l = 1.4$ m, and the unprocessed side of the fiber is connected to the optical setup used for optical access and readout. The MW signal is fed from a microwave source to the silver wires with a standard SMA-jack. We describe our presented device as an endoscope since it is designed to be able to detect ODMR measurements in space-constrained areas, which we can realize by the flexible optical fiber and an RF emitting structure on the tip featuring a diameter of the tip of $d = 2.5$ mm.

We point out that the application of the device presented here is not limited to magnetometry using NV centers. Harnessing the coherence properties of the NV-center, we show the working-principle of the fiber-tip antenna as a distance sensor based on the measurement of the Rabi frequency Ω in a pulsed ODMR measurement. Moreover, the device could also be employed in the coherent microwave control of Silicon-Vacancy (SiV) centers in diamond,^{23,24} Boron-Vacancy centers (VB^-) in hexagonal Boron-Nitride (hBN),²⁵ or Divacancies in Silicon-Carbide (SiC).²⁶ Furthermore, the fiber-tip antenna presented here could also be a powerful tool for precise microwave control of cold gases inside²⁷ or in close proximity to an optical fiber²⁸ as well as for the excitation of spin waves.²⁹

In the following, we detail the device fabrication using mDLW on the fiber facet. Moreover, we measure the antenna characteristics by means of scattering parameters and show that a high coupling of the magnetic field in close proximity is achieved. Finally, we investigate the device's sensing capabilities by applying it as an NV

magnetometer and distance sensor using cw and pulsed ODMR and compare it to a conventional microscope setup.

II. DEVICE FABRICATION

In order to fabricate a compact, robust endoscope with an integrated RF antenna on an optical multimode-fiber as an optical access port, we chose a design for the endoscope head that is similar to a typical fiber ferrule with a diameter size of 2.5 mm. The fabrication starts with a polytetrafluoroethylene (PTFE) mold in a cylindrical shape with 25 mm height and a diameter of 20 mm as shown as a half section schematic in Fig. 2(a). A bore hole with a drill diameter of 2.5 mm and a depth of around 22 mm is added centered in the lid surface of the cylinder. From the other side of the cylinder, three holes with a 0.3 mm drill are added, where one hole is also centered, and the two other holes are drilled in a 0.5 mm distance left and right from the center such that the three holes are aligned along the diameter of the cylindrical holder. Since PTFE is a relatively soft material, the actual size of the 0.3 mm bore holes is slightly smaller and perfectly fit a 200 μm silver wire (99.99% silver) and a 125 μm clad fiber with a 50 μm core diameter (Thorlabs FG050LGA) without significant clearance. The silver wires are subsequently added into the mold and taped to the sides to achieve a slightly V-shaped path such that cables are not in physical contact avoiding a short circuit. In the next step, a partially stripped fiber is added such that the end of the stripped part is roughly in the center of the mold. The 0.3 mm holes are sealed up with a removable gum-like glue (Fixogum) and filled with epoxy resin and hardener HT2 from R&G. During the 24 h curing process at room temperature, the fiber is fastened in a centered position at the top of the mold. A schematic half section image of the filled mold is shown in the left part of Fig. 2(a). After curing, the PTFE mold is sliced in half by sawing from both sides until the mold can carefully be broken and the epoxy with the fiber and silver cables is extracted. To improve the stability and avoid breaking of the fiber for the following process, shrink tubing is added to increase the stiffness and ensure electrical insulation between both silver wires. In the next step, the facet of the sensor head is polished on diamond polishing paper for optical fibers in a bare ferrule fiber polishing puck (D50-F) from

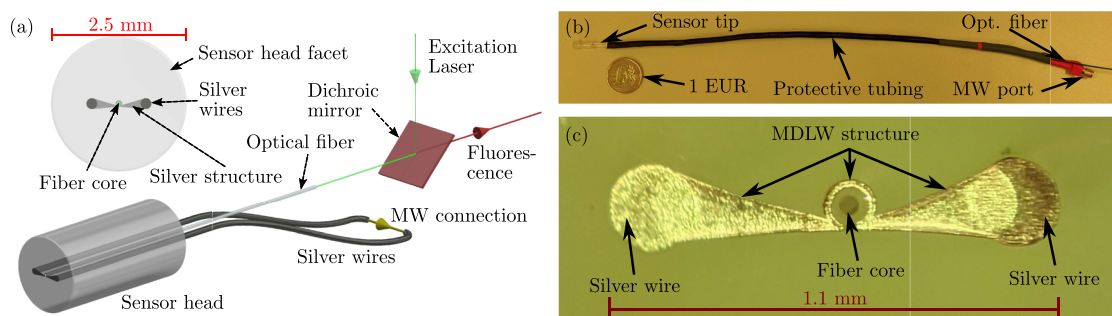


FIG. 1. Schematic of the fiber-tip endoscope antenna (a). A silver-based mDLW antenna is fabricated on the facet of an optical fiber and connected to additional silver wires. The MW signal is supplied to the cables via an SMA-jack, which is soldered to the silver wires. Optical access for excitation and read out of NV centers is provided by the multimode fiber. An image of the whole sensor including a one euro coin as a size reference is shown in (b). In (c), a microscopic image of the final silver structure on the sensor tip is depicted.

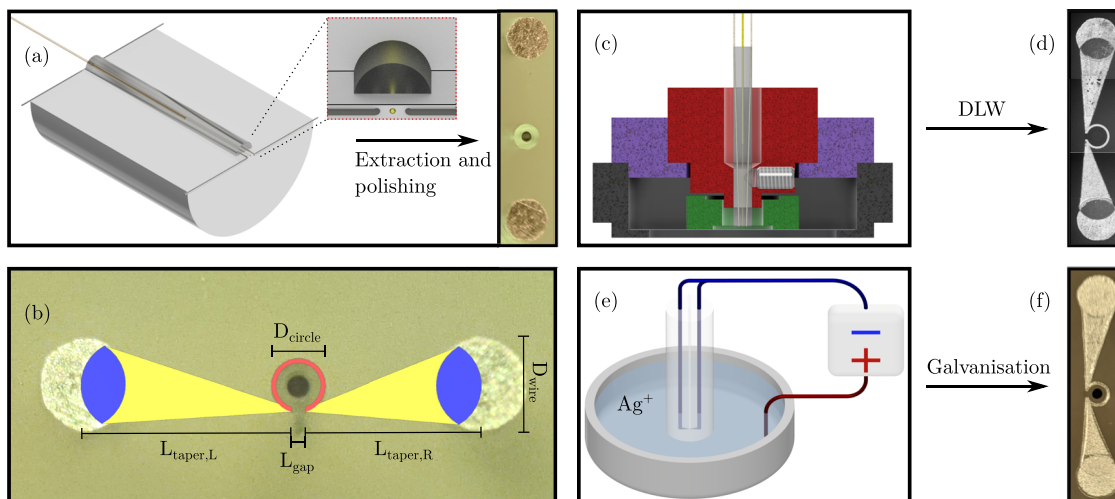


FIG. 2. The production of our endoscope starts with a PTFE mold for silver wires and fiber, which is shown in the left and central image in (a). The result after extraction and polishing of the sensor tip is shown in the right section of (a). (b) shows the geometrical construction and dimensions of the silver structure drawn over an image of the fiber facet, which is planned to be directly laser written on. The geometrical shape and size of the structure is adapted to the actual position of silver wires and the optical fiber core by taking images with the microscope system of the PPGT using the $20\times$, 0.5NA objective. For a scale reference, the calibrated stage of the PPGT is utilized. The red circle has an inner diameter of $100\ \mu\text{m}$ and an outer diameter of $D_{\text{circle}} = 120\ \mu\text{m}$ with a gap distance at the bottom of $L_{\text{gap}} = 30\ \mu\text{m}$ and is centered around the fiber core. As a connection between the circle and the outer silver wires, a taper structure (yellow) is created. The blue part of the structure marks the overlapping area between the taper structure and the silver wires. The values of the relevant sizes are $L_{\text{taper,L}} = 469\ \mu\text{m}$, $L_{\text{taper,R}} = 393\ \mu\text{m}$, and $D_{\text{wire}} = 200\ \mu\text{m}$. After creating the antenna structure, the fiber stays mounted in the special mount (c) for the DLW process, which was also used for taking the microscope images of the sensors tip with the PPGT. The resulting structure is shown in (d). Since this is a not well enough conducting structure a galvanization post process (e) is realized. The final structure is shown in (f).

Thorlabs preparing a flat surface for the direct laser writing process. The sensor's surface after polishing is shown on the right side in Fig. 2(a).

With the geometry given after polishing, we design an Ω -shaped antenna structure consisting of a circle with a gap connected by two tapers to the silver wires, as shown in Fig. 2(b). For the direct laser-writing process of such a structure, we employ a 2D silver resist consisting of silver-perchlorate, water, and trisodium citrate.³⁰ A special mount for the fiber, shown in Fig. 2(c), is holding the fiber in position during the writing process at a small distance of around $100\text{--}150\ \mu\text{m}$ above a glass substrate with the silver resist on top of it. In order to reduce the evaporation of the silver resist, an additional ring around the fiber and the silver resist is added and sealed with Fixogum. The writing process is carried out on a commercial Nanoscribe system (Photonic Professional GT, PPGT), which uses a femtosecond $780\ \text{nm}$ laser for two-photon reduction. Using an air objective ($20\times$, 0.5NA , Nanoscribe), we write the structure in three slices with a slicing distance of $1.5\ \mu\text{m}$ and hatched in $0.3\ \mu\text{m}$ steps with a writing speed of $200\ \mu\text{m/s}$. The two additional slices improve the structure density, where less silver was deposited due to the surface roughness of the fiber tip during the writing process or microscopic holes and cracks in the surface. The final silver structure consists of elementary silver and is developed by rinsing water over the sensor head and blow-drying with compressed air. The DLW structure connecting both silver wires and forming the antenna on the fiber facet is shown in Fig. 2(d). In general, the loop design for the mDLW antenna is given by two major considerations. First, the loop diameter is chosen such that it does not block

nor reflect light guided in the fiber core. Second, the loop is chosen as small as possible to achieve a high field in the center and a small penetration depth. With such a design, we expect to achieve a rapid change of the field amplitude (and as we show later, the Rabi frequency) when varying the distance between antenna and diamond without reducing the fluorescence collection. The thickness of the DLW structure is approximately on the order of below $1\ \mu\text{m}$, because the 2D resist cannot provide higher structures, and a 2.5D resist failed in producing sufficiently high quality structures due to overheating. Electrical resistance measurements after the development process of the structure show an ohmic resistance in the $\text{k}\Omega$ to $\text{M}\Omega$ range, which can be explained by the thin silver layer in combination with microscopic cracks and holes at borders between different materials and in the surface of the fiber tip. To improve the conductivity of the structure, an additional galvanization step is performed as depicted in Fig. 2(e). To this end, a commercial galvanization solution from Marawe is used. The solution consists of a silver-electrolyte and a surfactant for a smooth surface. The voltage in the galvanic solution is set to $0.8\ \text{V}$, and the structure is kept in the solution for $6\ \text{min}$ in total and then rinsed with water. A silver wire (99.99%) with a diameter of $200\ \mu\text{m}$ serves as a cathode. After galvanization, the final antenna structure, which is shown in Fig. 2(f), has an ohmic resistance of $R = 0.51\ \Omega$ measured through both silver wires and the structure itself with a digital multimeter (Keithley 2100 6 1/2 DIGIT MULTIMETER) after subtraction of the resistance of the connecting cables. The thickness of the silver structure z is subsequently measured with an optical microscope setup described below using an objective with a NA of 0.5 . The distance

z between the focus points of sharp images of the antenna surface and the fiber facet surface is used to estimate the thickness. Hereby, a thickness of the structure of about $z \approx 5 \mu\text{m}$ is determined.

For the optimization of the antenna's resonance frequency, the length of the silver wires are cut to a multiple of the wavelength λ_{res} at the resonance frequency of $f_{\text{res}} = 2.87 \text{ GHz}$ which corresponds to $\lambda_{\text{res}} \approx 104.46 \text{ mm}$. This underlines the statement that the sample that is examined lies in the near-field regime of the endoscope since the working distance of the endoscope is well below $d < 2\lambda_{\text{res}}$.³¹ Subsequently, the wires are soldered to an SMA-jack and the resonances of the antenna are measured with a vector network analyzer (VNA) MS2038C from Anritsu. The resonance frequency of the antenna is adjusted by modifying the length of the silver cables and measuring the frequency response using the VNA. Further shrink tubing and furcation tubing are then added to the whole cable length to reduce the flexibility of the device and increase the stability of all components and the resonance frequency of the antenna, which can shift due to external stress on the sensor or bending of the wires. In the last step, an FC/PC adapter is connected to the end of the optical fiber enabling a quick connection of the sensor to a laser source via a fiber coupler.

III. ANTENNA CHARACTERISTICS

As a first step for the characterization of the produced antenna structure the scattering parameter S_{11} , a value for the reflected power of the antenna is measured with the VNA. For S_{11} , a small value is desirable corresponding to a large fraction of the power irradiated from the antenna. For a two-port measurement, the scattering parameters determined by the VNA are defined as

$$\begin{pmatrix} b_1 \\ b_2 \end{pmatrix} = \begin{pmatrix} S_{11} & S_{21} \\ S_{12} & S_{22} \end{pmatrix} \begin{pmatrix} a_1 \\ a_2 \end{pmatrix}, \quad (1)$$

where a represents the incoming wave at each antenna, b the reflected wave and the index is the number of the port of the respective antenna. The reflection parameter S_{11} in the area of the expected resonance of an NV center around 2.87 GHz is shown in Fig. 3. We observe a reduction of the S_{11} parameter to -22 dB within a bandwidth (-3 dB) of $\Delta\nu_{1,-3\text{dB}} = 6.9 \text{ MHz}$ around a resonance frequency of $\nu_{1,\text{res}} = 2.846 \text{ GHz}$ of the antenna. Furthermore, we observe shifts in the order of few 10 MHz in the antenna's resonance frequency due to bending of the RF guiding silver wires and due to the presence of a close by detector, for example, a second antenna in close proximity, which is shown in Fig. 7 in Appendix A. In the proposed example application of magnetometry with NV centers, the Zeeman shift due to a magnetic bias-field is typically several orders of magnitude larger than the bandwidth of the antenna.⁵ Therefore, in broadband applications such as ODMR measurements with NV centers, antennas are often driven off resonance and we use the high field intensity in close proximity to the silver DLW structure to efficiently couple to the magnetic dipole transitions of the spin-states. We point out that due to the endoscope design, it is necessary to connect the mDLW structure with comparatively long silver wires parallel to the optical fiber. Therefore, the antenna including the connection wires cannot be electrically short, i.e., the length of the wire is in the order of the wavelength and shows a sharp resonance.

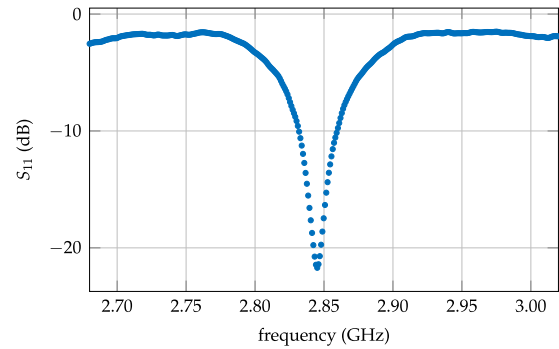


FIG. 3. The dependence of the experimental scattering parameter S_{11} on the frequency. The minimum occurs close to the aimed frequency to drive the NV centers' spin transitions at 2.87 GHz.

However, the design idea of the endoscope is to produce a high magnetic field on the fiber's tip in order to drive spin transitions. This is achieved by a high current flowing through the mDLW structure. Thus, we have chosen to match the antenna resonance to the center of the desired frequency range. This matching strategy ensures that a current node in the mDLW structure is as far away as possible in frequency space. Therefore, we achieve a current flow through the mDLW structure over the maximum possible frequency range given by the endoscope design. In addition to further measurements in Sec. V, which determine the microwave's magnetic field intensity as a function of distance to the antenna structure, a measurement of S_{21} is shown in Fig. 7 in Appendix A. Since measurements with a VNA, such as the ones shown additionally in Fig. 7, cannot fully distinguish between the electrical or magnetic field components and macroscopic antennas cannot be considered as point-like, we utilize diamonds containing NV centers and Rabi oscillations as a detection method to characterize the distance dependence of the magnetic field intensity emitted by the antenna, which is described in detail in Sec. V. In the course of these measurements, we have verified that the antenna properties are unchanged, if powers of up to 40 dBm are applied in measurements taken over a period of several weeks in total.

IV. TEST SETUP FOR MEASUREMENTS WITH NV CENTERS

In order to test the device produced, we employ additionally a microscope for NV magnetometry as depicted in Fig. 4. The sample examined consists of a glass substrate with $15 \mu\text{m}$ -sized microdiamonds hosting NV centers with a doping of $c_{\text{NV}} = 3.5 \text{ ppm}$ from Adamas Nanotechnologies. The NV center is a paramagnetic, optically active point defect in the diamond lattice composed of a substitutional nitrogen atom (N) and an adjacent vacant lattice site (V).⁵ This defect features local energy levels in the diamond's band-gap, which can be addressed with optical and microwave wavelengths, as depicted in the level-scheme in Fig. 4. Its ground state splits into a spin-triplet with $D = 2.87 \text{ GHz}$ zero-field splitting between the $m_s = 0$ and degenerate $m_s = \pm 1$ spin states, quantized along the NV-axis. This $m_s = \pm 1$ degeneracy is split by crystal strain E and

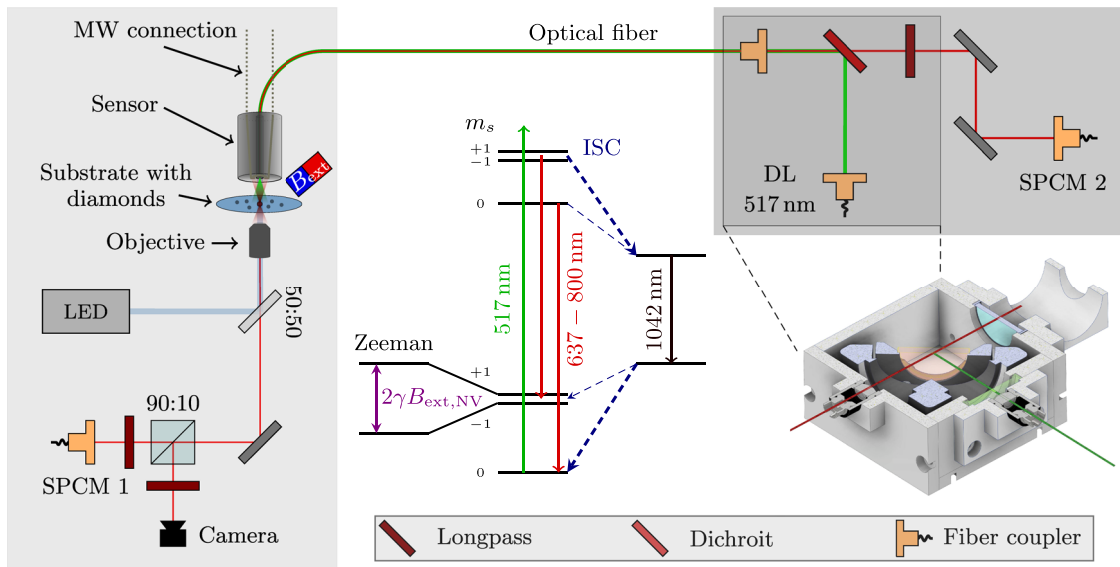


FIG. 4. Overview of the measurement setup including the level scheme of the NV^- center. A diode laser (DL) is coupled into the optical fiber of the endoscope and microwaves are applied to the mDLW-antenna at the MW connection wires. The fluorescence light of NV-centers in a single-crystalline microdiamond is either gathered with the microscope objective into the confocal beam path or with the endoscope. In both paths, the fluorescence light is transmitted to a fiber-coupled single-photon counting module (SPCM). This setup enables simultaneous detection in both beam-paths and, therefore, a comparison between confocal microscope and endoscope.

the presence of an external magnetic field \vec{B}_{ext} . In the experimental setup, we apply a permanent magnet fastened a few centimeters away from the sample as an external static magnetic field source. Ground-state splitting and Zeeman shift, caused by the magnetic field component along the NV-axis, can be described by the spin Hamiltonian,^{1,5}

$$H = hDS_z^2 + hE(S_x^2 - S_y^2) + \gamma\vec{S} \cdot \vec{B}_{\text{ext}}, \quad (2)$$

where h is the Planck constant, $\vec{S} = (S_x, S_y, S_z)^T$ is the vector of the Pauli matrices and $\gamma = \mu_B g_s / h$ is the splitting constant with the Bohr magneton μ_B and Lande-factor g_s . The optically excited state is energetically separated by 1.945 eV corresponding to a zero phonon line (ZPL) at $\lambda_{\text{ZPL}} = 637$ nm. The line is strongly broadened by phononic states of higher energy allowing for off-resonant excitation at room temperature. Thus, the excited states can decay under the emission of a photon in the phonon-broadened band ranging from 637 to 800 nm. Furthermore, a second decay path via intersystem-crossing (ISC) into long-lived singlet states and a subsequent second ISC back to the triplet ground state exists, leading to infrared emission of 1042 nm outside the measured fluorescence band. The $m_s = \pm 1$ -states preferably decay via this path, and, therefore, optical pumping leads to spin-polarization into the $m_s = 0$ ground state. The same mechanism is harnessed for optical magnetic resonance (ODMR) of the spin states under resonant microwave excitation. Here, the spin-polarized NV centers are subject to a coherent manipulation of the ground state via microwaves in the range of 2.87 GHz reducing the optical fluorescence dependent on the spin state population.^{1,5}

The fabricated fiber-tip endoscope is precisely positioned in close proximity to a single-crystalline microdiamond using the camera of the wide-field microscope in combination with three linear stages in an x,y,z combination. The optical fiber itself is mounted in a machined tube for increased stability, which is attached to the three linear stages. A microwave setup for cw and pulsed excitation is connected with the Sub-Miniature version A (SMA)-jack of the antenna produced. For all measurements shown in the main text, we use a microwave generator from Rhode and Schwarz (SMBV100A) together with a microwave amplifier from Mini-Circuits (ZHL-16W-43-S+) with a maximal power output of 16 W. Moreover, a laser source (DLnsec 520, LABS electronics) with a wavelength of $\lambda = 517$ nm, which can be operated in cw and pulsed mode is fiber-coupled to the connection box and coupled into the endoscope with a dichroic mirror (DMLP 605, Thorlabs). Therefore, the fiber-tip endoscope can drive optical as well as microwave transitions of NV centers. Furthermore, the optical response in ODMR measurements, i.e., the intensity of the fluorescence light, is collected via the fiber-endoscope as well as with the confocal microscope configuration. In the confocal beam path, we employ a longpass-filter (FELH650, Thorlabs) to transmit NV-fluorescence to a fiber-coupled single-photon counting module (SPCM, Count-T-100, laser components) for detection. The light collected by the fiber-tip endoscope is guided back into the connection box, and NV fluorescence is transmitted through the dichroic mirror and additionally filtered by a longpass-filter (FELH 650). Furthermore, the fluorescence light is measured either directly with a photodiode, or by applying a fiber-coupled sensor, which is a second SPCM (Count-T-100, laser components) in our setup. All optics connected to the fiber-tip endoscope for excitation and read-out of NV centers can be mounted in the small

connection box and accessed via multiple optical fibers. This leads to a portable device enabling quick exchanges of individual filters, excitation lasers, and detectors. The whole configuration allows simultaneous detection and comparison of the ODMR signal gathered with the fiber and the confocal microscope. Furthermore, all our experiments were carried out at room temperature under lab conditions.

V. DEVICE PROPERTIES

A. CW ODMR

We apply the fiber-tip endoscope to record a spectrum of the electron spin resonances of NV centers in an arbitrary external magnetic field via continuous-wave ODMR, using a cw laser source and sweeping the microwave frequency across the resonances.

Using the endoscope fiber, we record the fluorescence intensity I with and without applying the external microwave field through the endoscope antenna, and calculate the relative fluorescence level detected with the endoscope and the microscope simultaneously. The relative fluorescence dependence on the MW frequency f_{MW} is calculated for each device as

$$R(f_{MW}) = \frac{I_{MWon}}{I_{MWoff}}, \quad (3)$$

where the index denotes if the state of the microwave source is turned on or off. The relative fluorescence level dependence on the MW frequency yields an ODMR spectrum, which is fully excited and measured through the fiber. Such a spectrum is presented in Fig. 5(a).

We observe eight resonances corresponding to four NV-axes with two spin-transitions $m_s = 0 \iff m_s = -1$ and $m_s = 0 \iff m_s = +1$ with both detection devices, i.e., the microscope and the fiber endoscope. This verifies that the microdiamond comprises a single crystal. Furthermore, we observe a feature in the fluorescence spectrum around 2.80 GHz, which we attribute to the sharp resonance of the antenna (see Sec. III) being in close proximity to the spin resonances and resulting in power-broadening.

The small shift of the antenna's resonance frequency with respect to the resonance frequency shown in Fig. 3(a) might stem from a different bending of the connection wires and the dielectric glass substrate placed at a small distance to the antenna. So far, we have verified that ODMR can be achieved with the fabricated endoscope. However, the benefit of the DLW structure connecting the wires for sensing applications has not been discussed. Therefore, we have compared the fabricated device to another endoscope, where the DLW process has been omitted, i.e., the two silver wires are not connected by a DLW structure, in Appendix B. We observe almost no ODMR signal from such a device when employing a tip of an endoscope without a silver structure, connecting the two wires, as shown in Fig. 8(a) to the same diamond under similar conditions. This observation is in accordance with our expectation that the current within the metallic DLW structure mainly contributes to the magnetic field component at the diamond's position below the fiber core. We deduce that a high coupling of the magnetic field component can thus be achieved with the presented device housing the DLW structure on the fiber-facet.

An important figure of merit to evaluate and compare the performance of the fiber endoscope is the magnetic field sensitivity η . This quantity is usually compared using an individual resonance i and is defined as³²

$$\eta_i = P_L \frac{1}{g_s \mu_B} \frac{w_i}{C_i \sqrt{R}}, \quad (4)$$

where $P_L = \frac{4}{3\sqrt{3}}$ is a factor for the maximum slope of a Lorentzian profile, w_i is the width and C_i is the relative fluorescence contrast of the respective resonance and R is the photon-count rate. Here, the width w and relative fluorescence contrast C depend on the driving-field strengths of the laser and microwave antenna, which can be optimized to achieve a minimum, i.e., an optimal sensitivity. The photon-count rate R depends on the laser-intensity and total photon-collection efficiency. Neglecting the effects of residual fiber fluorescence and experimental imperfections, we estimate a ratio of total collection efficiency of 5:1 between confocal setup and fiber-tip endoscope given by the different numerical apertures

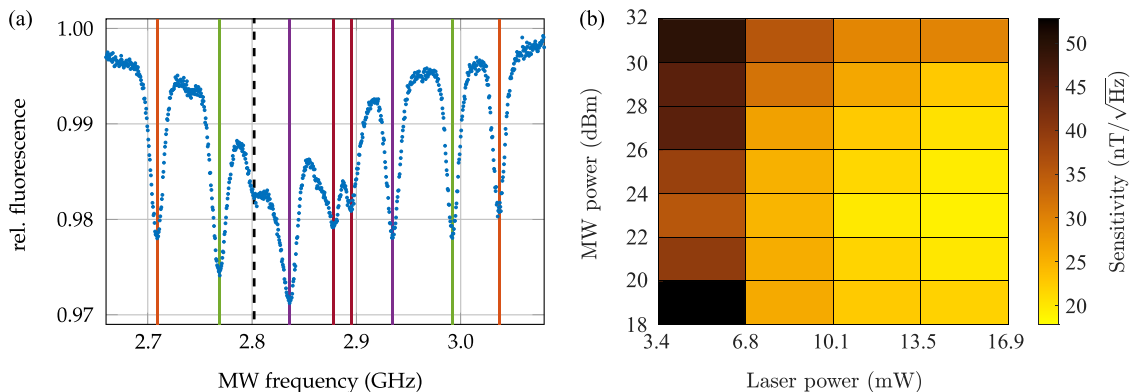


FIG. 5. (a) ODMR spectrum of a single-crystalline microdiamond in an external magnetic field measured through the optical fiber. Eight resonances corresponding to the two spin transitions and four crystal axes are observed. Resonances of the same crystal axis are highlighted in the same color. Additionally, a ninth resonance at the fiber-tip antenna's resonance is observed in the spectrum (black dashed line). (b) Calculated sensitivity dependence on Laser and MW power of the resonance at 2.71 GHz measured through the optical fiber.

($NA_{\text{Microscopeobjective}} = 0.50$; $NA_{\text{Endoscope}} = 0.22$). A direct comparison between the fluorescence intensity coupled to the microscope objective and the fiber-tip endoscope shows a ratio of 6:1, measured directly in the beam path with a power meter. This ratio is close to the expected value of 5:1, which we calculate in Appendix C. The subsequent fiber-coupling to the SPCMs, however, is achieved in two distinct ways. In the microscope beam path, the fiber-coupling to the SPCM is accomplished by a chromatically corrected microscope objective. By contrast, in the beam path after the endoscope, conventional chromatically uncorrected fiber-couplers are used to couple light out of the endoscope fiber and to realize a fiber-coupling of the SPCM. This leads to a worse fiber-coupling efficiency one order of magnitude below the coupling with the objective. We attribute this difference mainly to chromatic aberrations, which are partially uncorrected in the broad emission range of NV centers (600–800 nm). In total, the photon count rate is 70.3 times higher when using the confocal microscope. We emphasize that this vast difference does not stem from the presented endoscope itself and could be overcome either by employing chromatically corrected fiber-couplers or by using non-fiber-coupled detectors. In the following, we did not further improve the coupling efficiency since both beam paths yield a photon flux well above the saturation limit of the SPCMs. For instance, additional ND filters ($OD_{\text{Microscope}} = 7.1$ and $OD_{\text{Endoscope}} = 5.6$) were used to stay below the saturation limit. We point out that the fluorescence intensity coupled to the fiber endoscope from a 15 μm -sized diamond is high enough to be measured with an inexpensive photodiode as shown in Appendix D. After optimization of laser and microwave power to the resonance at 2.7145 GHz, we achieve a sensitivity of $\eta_{\text{CM}} = 2.1 \text{ nT}/\sqrt{\text{Hz}}$ using the confocal microscope and $\eta_{\text{FT}} = 17.8 \text{ nT}/\sqrt{\text{Hz}}$ using the fiber-tip endoscope, respectively. In conclusion, compared with the microscope setup, our endoscope achieves sensitivities that differ by less than one order of magnitude due to the light coupling efficiency of both systems.

B. Pulsed ODMR

We use coherent Rabi oscillations in pulsed ODMR sequences to measure the coupling strength of the magnetic microwave field to the NV centers' spins as dependent on the distance of fiber tip and microdiamond. The fiber-tip endoscope is precisely positioned, i.e., the fiber core is centered in x and y directions above a microdiamond, with the wide-field microscope setup using an objective with a 2.1 mm working distance and a depth of field of 4.2 μm at 650 nm. Due to the Zeeman splitting caused by the positioned permanent magnet, a single resonance is driven with the microwave, while all other resonances are far detuned from the microwave frequency such that we can approximate (secular approximation) the NV ensemble along one crystal axis as a two-level system. We control the distance between the endoscope's facet bearing the antenna and the microdiamond on a glass substrate using the microscope setup's motorized stage to infer the distance between sharp images of the antenna and the diamond. At each distance, we use pulsed ODMR to measure coherent Rabi oscillations of a single magnetic-field-split resonance with the sequence depicted in Fig. 6(a). The envelope of the rectangular microwave pulse is generated with digital In-phase and Quadrature-modulation (IQ) and the amplitude of the signal is set constant at 37 dBm directly at the output of the microwave amplifier. Typical measurement data are shown in Fig. 6(b). We infer the Rabi frequency Ω , which is proportional to the field B_{MW} produced by the antenna at the microdiamond's position from a fit function according to

$$f(t_{\text{MW}}) = y_0 + A \cos(2\pi\Omega t_{\text{MW}} + \phi_0) \exp(-t_{\text{MW}}/\tau), \quad (5)$$

of each dataset, where y_0 is the offset, Ω is the Rabi frequency, ϕ_0 is a phase offset due to pulse imperfections, and τ is the dephasing time of the spin ensemble during the Rabi cycle. The resulting Rabi frequency Ω as a function of the distance is plotted in Fig. 6(c). The

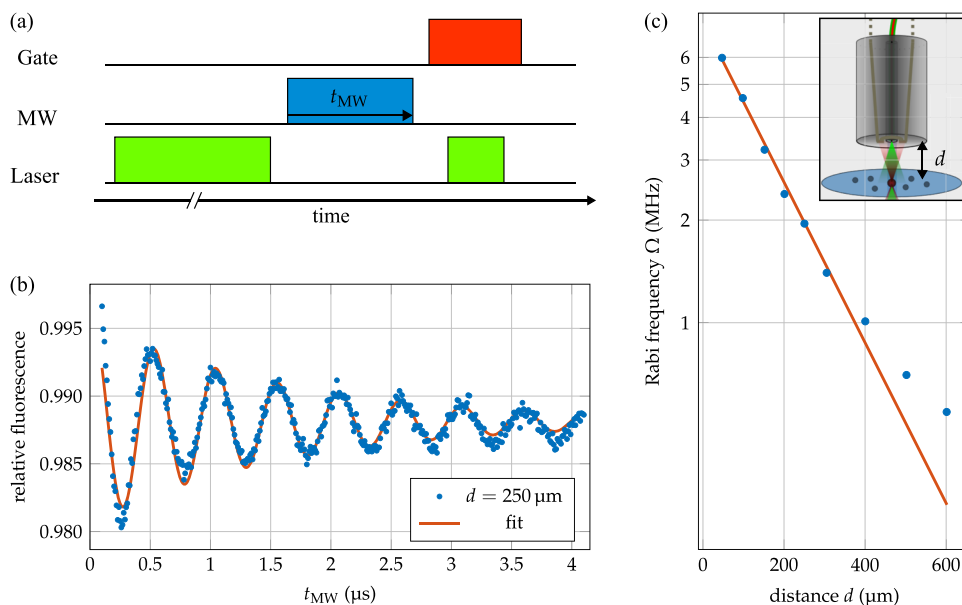


FIG. 6. Dependence of the Rabi frequency on the distance of the antenna to the sample. (a) Pulse sequence of the Rabi cycle, (b) Rabi oscillations for a distance of $d = 250 \mu\text{m}$ and fit curve to extract the Rabi frequency Ω , (c) Extracted Rabi frequencies as a function of the distance d and exponential fit; the inset shows a zoom-in to the measurement setup where the distance d between the sample and the antenna is varied. The errors from the fit and the assumed measurement errors for the distance are smaller than the size of the data points. The microwave generator was set to a frequency of 2.7145 GHz for the Rabi oscillation measurement shown, corresponding to a resonance of the ODMR spectrum recorded.

influence of detuning due to neighboring resonances is neglected since closest resonance frequency in the ODMR spectrum can be found at 2.77 GHz resulting in an effective cross section smaller than $\sigma \approx 1.9 \times 10^{-3}$ leading to a negligible amplitude for the excitation of nearby resonances. We observe a reduction of the Rabi frequency with increasing distance following phenomenologically an exponential law for small distances. The measured Rabi-frequency depends on the magnetic microwave field strength along the NV-axis and will, therefore, change for other orientations within the crystal. We point out that the pulsed measurement scheme using Rabi oscillations could be applied to infer an unknown distance if the device is calibrated beforehand.

VI. CONCLUSION AND OUTLOOK

In conclusion, we have presented the production of an electrical antenna on the facet of a multi-mode glass fiber using mDLW. The device combines electrical connections as well as optical access through the fiber on a diameter of the complete package of $d = 2.5$ mm. We have investigated the antenna characteristics by means of scattering parameters and found a high magnetic-field coupling in the near field. The device has been applied in a microscope setup for microdiamonds containing NV centers as an endoscope delivering optical and microwave excitation and guiding the fluorescence signal.

In comparison to a conventional microscope, the size of the integrated fiber-tip antenna is reduced by two orders of magnitude and can be further miniaturized. The magnetic field sensitivity of $17.8 \text{ nT}/\sqrt{\text{Hz}}$ is decreased in comparison to a microscope setup by one order of magnitude due to the coupling, lower numerical aperture, and losses in the fiber. The sensitivity measured with the fiber-tip endoscope can be further improved, i.e., decreased, by increasing the count rate. A simple approach would be to use a fiber with a higher numerical aperture. Another option would be to use a lensed fiber facet, which could be created e.g., with DLW of a low-fluorescent and transparent polymer photoresist. A Fresnel-lens design could be harnessed to keep a flat surface to employ the fiber as a distance sensor at small distances. Furthermore, immersion oil could be used to effectively increase the numerical aperture as used for oil microscope objectives. In a complementary approach to mapping of antenna near fields on a sample plane with NV-centers,³³ we have measured the reduction of the magnetic near field for varying distances in the micrometer regime. Using a pulsed sequence for the optical detection of Rabi oscillations, the device allows one to measure distances as a function of the Rabi frequency by mapping a Rabi frequency, which depends on the RF power at a given RF frequency to a distance between RF emitting structure and diamond containing NV centers. We point out that the non-linear increase of the measured Rabi frequency with decreasing distance leads to higher precision for smaller distances.

Furthermore, we have shown one possibility of tuning our antenna's resonance frequency by changing the length of the silver wires. Having such a sharp resonance, which is predominantly given by the design choice, can be especially favorable in systems where RF excitations in a small bandwidth are needed. Specifically, such a fiber-integrated antenna could extend the work on fiber-based cold atom studies^{27,28} by microwave near fields for hyperfine manipulation. However, we conclude from the ODMR spectra measurements

in Figs. 5, 8, and 10 that even if the sample is excited off-resonantly to the antenna's resonance, an excitation is possible at usual powers. We find from our results that having an electrically guiding structure in the near field of a diamond containing NV centers can overcome or at least reduce the need for having an antenna emitting in a broad band. Simultaneously this enables endoscopic measurements on diamonds containing NV centers as presented in this work. Further optimization of the mDLW structure, the galvanization, and connection wires could allow enhancements of the bandwidth for this purpose.

ACKNOWLEDGMENTS

We acknowledge support by the nano-structuring center NSC. This project was funded by the Deutsche Forschungsgemeinschaft (DFG, German Research Foundation)—Project-ID No. 454931666 as well as via the CRC 926 MICOS Project-ID No. 172116086 subproject B11. Furthermore, we thank Dennis Lönard and Isabel Manes for helpful discussions and experimental support.

AUTHOR DECLARATIONS

Conflict of Interest

The authors have no conflicts to disclose.

Author Contributions

Stefan Dix: Conceptualization (equal); Data curation (equal); Formal analysis (equal); Investigation (equal); Methodology (equal); Software (equal); Validation (equal); Visualization (equal); Writing – original draft (equal); Writing – review & editing (equal). **Jonas Gutsche:** Conceptualization (equal); Data curation (equal); Formal analysis (equal); Investigation (equal); Methodology (equal); Software (equal); Validation (equal); Visualization (equal); Writing – original draft (equal); Writing – review & editing (equal). **Erik Waller:** Methodology (supporting); Resources (supporting). **Georg von Freymann:** Methodology (supporting); Resources (supporting). **Artur Widera:** Conceptualization (equal); Funding acquisition (equal); Project administration (equal); Supervision (equal); Writing – original draft (equal); Writing – review & editing (equal).

DATA AVAILABILITY

The data that support the findings of this study are available from the corresponding author upon reasonable request.

APPENDIX A: TWO-PORT MEASUREMENTS WITH TWO ANTENNAS IN CLOSE PROXIMITY

In addition to the S_{11} parameter measurement, shown in Fig. 3, we also measure the scattering parameters S_{11} and S_{21} in a two-port measurement for varying distances between the fiber-tip antenna produced (1) and a reference loop antenna (2) with a circumference of $l = \lambda_{\text{MW}} \approx 10$ cm and resonance frequency of $\nu_{2,\text{res}} = 2.87$ GHz, which is shown in Fig. 7. Specifically, S_{21} represents the transmitted power from the antenna produced into the reference loop antenna.

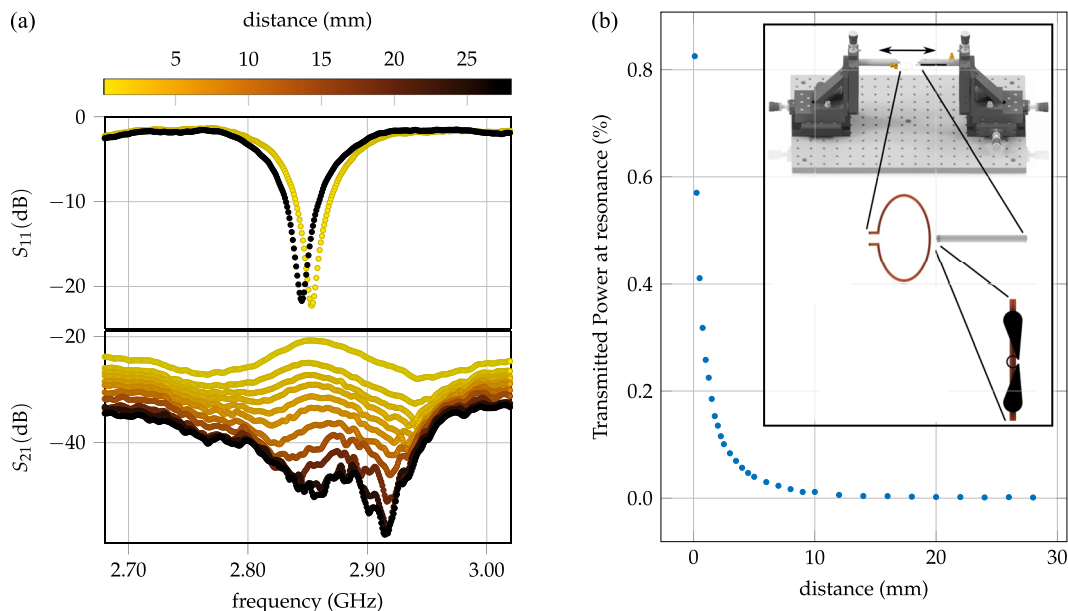


FIG. 7. Experimental scattering parameters. (a) Dependence of S_{11} and S_{21} parameters on the distance between the manufactured antenna on the fiber-tip to a reference λ loop antenna. (b) Dependence of transmitted power at the resonance of the fiber-tip antenna on the distance. The inset shows the measurement setup and relative antenna alignment. Both antennas are oriented such that the taper- and omega-structure of the produced antenna and the antenna connected to port two meet each other at the tip, while the taper- and omega structure is parallel to the wire of the antenna of port two.

A schematic of the measurement setup for both antennas is presented in the inset of Fig. 7(b). The smallest distance between both antennas spans the positions of the highest current at the resonance frequency in each antenna. Therefore, the coupling of the magnetic near field is expected to be the dominant contribution to the measured transmission, i.e., the S_{21} parameter. The distance between both antennas was set to zero by bringing both antennas to a visible contact where only the coating of the second antenna around the copper wire separates both antennas. We measure the S_{21} -parameter for varying distances between both antennas to track the distance dependence of the transmitted power in the near field. The measurement data are shown in Fig. 3(a), the data points at the resonance frequency $\nu_{1, \text{res}} = 2.846$ GHz are plotted vs the distance in Fig. 3(b). We observe a rapid reduction of the transmitted power with increasing distance at small distances. We, therefore, conclude that the produced fiber-tip antenna transmits a relatively high amount of the power in close proximity to the antenna. However, at such small distances both antennas cannot be assumed to be point-like magnetic dipoles. Hence, this measurement is prone to errors in comparison to the proposed application, where only the magnetic field component emitted by the antenna drives a spin transition.

APPENDIX B: COMPARISON TO A DEVICE WITHOUT DLW STRUCTURE

In order to analyze the benefit of the DLW structure connecting the silver wires of the fiber-tip endoscope, we compare it to a device lacking the DLW step in production. In Fig. 8(a), we show the facet of such an endoscope.

We have measured the reflection coefficient S_{11} of the fiber without the metallic DLW connection and show the measurement data in Fig. 8(b). The resonance frequency is $\nu_{\text{res}} = 2.909$ GHz, and the minimum value for the reflection coefficient is $S_{11}(f) = -14$ dB. The bandwidth amounts to $\Delta\nu_{\text{res}, -3\text{dB}} = 21.8$ MHz. In comparison to the endoscope featuring the DLW connection (see Sec. III), the resonance frequency is also in close proximity to the NV centers' resonance. Moreover, the scattering parameter S_{11} does not show such a strong reduction and a slightly larger 3 dB-width. We conclude that the electrical resonance of the antenna is mainly given by the silver wires.

Furthermore, we have applied both endoscopes as an antenna for measuring an ODMR spectrum in the absence of a magnetic field. In this case, we used the microscope setup for optical excitation and detection. We only applied the endoscope as an antenna to rule out an impact on the results due to other differences in excitation or detection efficiency. We used the same laser power, MW amplitude, and distance between fiber facet and diamond for this comparison. The resulting ODMR spectra are shown in Fig. 8(c). We observe the expected two resonances in the absence of a static magnetic field for the endoscope with a DLW structure. For the endoscope without such a structure, we observe an almost flat line and no reduction of fluorescence within the noise of the measurement. We have further increased the MW amplitude to 40 dBm (by a factor of 6.3) and repeated the measurement. In this case, a very small reduction of the intensity can be observed, which is still much less than observed with the endoscope housing the DLW structure. We, therefore, conclude that the current in the DLW structure is mainly contributing to the microwave's magnetic field component for such small distances. This enables an efficient microwave excitation of spin states due to

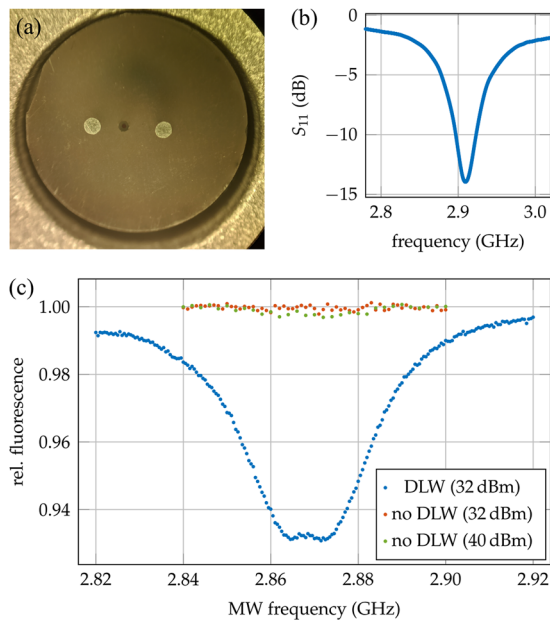


FIG. 8. (a) Facet of a fiber-tip endoscope without DLW structure. (b) Scattering parameter S_{11} of such an endoscope measured with a VNA. (c) Comparison of ODMR-spectra taken with the endoscope featuring the DLW connection (blue) and without such a structure at different microwave power (orange, green).

the metallic DLW structure reducing the applied microwave power needed to drive the spin states.

APPENDIX C: PHOTON COUNT RATE

When comparing the produced endoscope with the microscope setup, the main difference in performance is given by the photon collection efficiency. In the following, we detail the calculation of the theoretical ratio between the coupling efficiencies of the fiber and the microscope objective as shown in the sketch in Fig. 9.

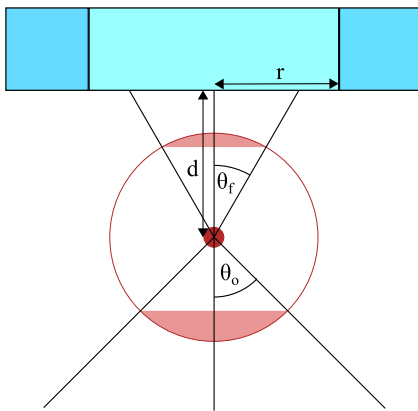


FIG. 9. 2D sketch showing the calculation of coupling efficiency into the fiber and objective.

First, we treat the microdiamond as an isotropic and point-like emitter. Both assumptions do not strictly hold since a microdiamond has an average size of $15 \mu\text{m}$ and the emission pattern of an NV ensemble in a single crystal diamond is given by two crossed dipoles perpendicular to each NV axis,³⁴ which are unknown for the diamond under investigation. Second, we assume that the fiber with core radius r is positioned at a small distance d to the point source such that the numerical aperture $NA_f = 0.22$ limits the collection efficiency into the fiber. This distance $d_{NA \text{ limit}}$, below which the numerical aperture is the limiting factor, is calculated by solving

$$NA_f = \sin \theta_f < \frac{r}{\sqrt{r^2 + d^2}}, \quad (\text{C1})$$

for the distance d . We calculate $d_{NA \text{ limit}} < 110.9 \mu\text{m}$, which can be achieved experimentally. At the same time, we assume that the point source is in the focal spot of the microscope objective such that the numerical aperture of $NA_o = 0.50$ limits the collection efficiency in the microscope beam path. Under the assumption of isotropic emission, the ratio of coupling efficiencies κ is then given by the ratio of the spherical caps' surface defined by the numerical apertures. This amounts to

$$\kappa = \frac{1 - \cos(\arcsin(NA_{\text{fiber}}))}{1 - \cos(\arcsin(NA_{\text{objective}}))} \approx 0.183 \approx \frac{1}{5.47}. \quad (\text{C2})$$

We have measured this ratio also experimentally by inferring the fluorescence intensity with a power meter in the setup shown in Fig. 4. The power was measured in front of the fiber coupling to SPCM 2 and in front of the fiber coupling to SPCM 1. The 50:50 beam splitter for white-light illumination was removed from the beam path during this measurement. Taking the 90:10 beam splitter into account, we observe an experimental coupling ratio of

$$\kappa_{\text{exp}} = \frac{P_f}{P_o} = \frac{2.072 \mu\text{W}}{0.326 \mu\text{W}} \approx 0.157 \approx \frac{1}{6.36}. \quad (\text{C3})$$

In this measurement, the power meter was set to a wavelength of $\lambda_{\text{PM}} = 680 \text{ nm}$, which is approximately the maximum wavelength in the fluorescence spectrum of NV centers. The additional losses in the measurement using the SPCMs can, therefore, be traced to different fiber coupling efficiencies in the subsequent fiber couplings. As mentioned in the main text, these losses were not further optimized since power needed to be further reduced in order to avoid saturation of the SPCMs.

APPENDIX D: ODMR MEASUREMENT WITH A PHOTODIODE

Instead of using an SPCM with several gray filters to avoid saturation of the device, we also applied a photodiode to detect the NV centers' fluorescence of a single microdiamond. The excitation laser light and MW signal are supplied continuously, and the MW frequency is ramped linearly from 2.7 to 3.0 GHz in 1.5 s and is limited by the minimal time step of the microwave generator [SynthHD (v2) from Windfreak Technologies]. The generated RF signal is amplified by an RF amplifier from Mini-Circuits (ZHL-16W-43-S+). For this measurement, a different diamond sample from the same type of microdiamond ($15 \mu\text{m}$) was utilized. The magnet was positioned slightly differently, resulting in a different

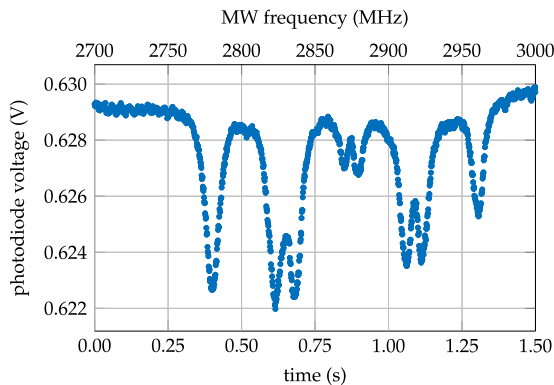


FIG. 10. ODMR spectrum taken with a photodiode (DET36A/M from Thorlabs). The parameters for the sweep of the microwave were stepping time $t_{\text{step}} = 4$ ms and step width $w_{\text{freq}} = 0.8$ MHz.

static magnetic field strength and thus, a different Zeeman splitting. The photodiode signal (voltage) measuring the spin-dependent fluorescence is monitored on an oscilloscope. The measured ODMR signal is shown in Fig. 10. We observe the typical eight resonances produced by a single crystalline diamond. To correlate the time-dependent x-axis to a frequency-dependent axis, the distances between the corresponding resonances $m_s = 0$ to $+1$ and $m_s = 0$ to -1 are fitted for each NV-axis as a time difference. With the chosen step time and step width, we convert the time distance between resonances to frequency differences leading to a frequency-dependent x-axis with an unknown offset. By modeling all possible resonance frequencies for all NV-axis orientations and external magnetic field orientations and subsequently comparing the distance between the resonance positions (measured and modeled), we are able to find fixed points for the resonances. These are then used to calculate the offset of the frequency-dependent x-axis.

REFERENCES

- L. Rondin, J.-P. Tetienne, T. Hingant, J.-F. Roch, P. Maletinsky, and V. Jacques, *Rep. Prog. Phys.* **77**, 056503 (2014).
- A. Boretti, L. Rosa, J. Blackledge, and S. Castelletto, *Beilstein J. Nanotechnol.* **10**, 2128 (2019).
- G. Kucsko, P. C. Maurer, N. Y. Yao, M. Kubo, H. J. Noh, P. K. Lo, H. Park, and M. D. Lukin, *Nature* **500**, 54 (2013).
- G.-Q. Liu and X.-Y. Pan, *Chin. Phys. B* **27**, 020304 (2018).
- M. W. Doherty, N. B. Manson, P. Delaney, F. Jelezko, J. Wrachtrup, and L. C. L. Hollenberg, *Phys. Rep.* **528**, 1 (2013).
- Y. Zhang, X. Wang, J. Wang, D. Zheng, L. Niu, X. Chai, J. Tang, H. Guo, L. Qin, X. Zhang, Z. Ma, J. Liu, Y. Sugawara, and Y. Li, *Jpn. J. Appl. Phys.* **60**, 092007 (2021).
- J. Tisler, G. Balasubramanian, B. Naydenov, R. Kolesov, B. Grotz, R. Reuter, J.-P. Boudou, P. A. Curmi, M. Sennour, A. Thorel, M. Börsch, K. Aulenbacher, R. Erdmann, P. R. Hemmer, F. Jelezko, and J. Wrachtrup, *ACS Nano* **3**, 1959 (2009).
- D. Terada, T. F. Segawa, A. I. Shames, S. Onoda, T. Ohshima, E. Ōsawa, R. Igarashi, and M. Shirakawa, *ACS Nano* **13**, 6461 (2019).
- D. Budker and M. Romalis, *Nat. Phys.* **3**, 227 (2007).
- I. K. Kominis, T. W. Kornack, J. C. Allred, and M. V. Romalis, *Nature* **422**, 596 (2003).
- D. A. Keder, D. W. Prescott, A. W. Conovaloff, and K. L. Sauer, *AIP Adv.* **4**, 127159 (2014).
- E. V. Levine, M. J. Turner, P. Kehayias, C. A. Hart, N. Langellier, R. Trubko, D. R. Glenn, R. R. Fu, and R. L. Walsworth, *Nanophotonics* **8**, 1945 (2019).
- D. Bai, M. H. Huynh, D. A. Simpson, P. Reineck, S. A. Vahid, A. D. Greentree, S. Foster, B. C. Gibson, and H. Ebendorff-Heidepriem, *APL Mater.* **8**, 081102 (2020).
- G. Chatzidrosos, J. S. Rebeirro, H. Zheng, M. Omar, A. Brenneis, F. M. Stürner, T. Fuchs, T. Buck, R. Rölver, T. Schneemann, P. Blümler, D. Budker, and A. Wickenbrock, *Front. Photonics* **2**, 732748 (2021).
- M. M. Dong, Z. Z. Hu, Y. Liu, B. Yang, Y. J. Wang, and G. X. Du, *Appl. Phys. Lett.* **113**, 131105 (2018).
- D. Duan, V. K. Kavatamane, S. R. Arumugam, Y.-K. Tzeng, H.-C. Chang, and G. Balasubramanian, *Appl. Phys. Lett.* **116**, 113701 (2020).
- I. V. Fedotov, S. M. Blakley, E. E. Serebryannikov, P. Hemmer, M. O. Scully, and A. M. Zheltikov, *Opt. Lett.* **41**, 472 (2016).
- A. Kuwahata, T. Kitaizumi, K. Saichi, T. Sato, R. Igarashi, T. Ohshima, Y. Masuyama, T. Iwasaki, M. Hatano, F. Jelezko, M. Kusakabe, T. Yatsui, and M. Sekino, *Sci. Rep.* **10**, 2483 (2020).
- F. M. Stürner, A. Brenneis, T. Buck, J. Kassel, R. Rölver, T. Fuchs, A. Savitsky, D. Suter, J. Grimmel, S. Hengesbach, M. Förtsch, K. Nakamura, H. Sumiya, S. Onoda, J. Isoya, and F. Jelezko, *Adv. Quantum Technol.* **4**, 2000111 (2021).
- D. Labanowski, V. P. Bhallamudi, Q. Guo, C. M. Purser, B. A. McCullian, P. C. Hammel, and S. Salahuddin, *Sci. Adv.* **4**, eaat6574 (2018).
- E. H. Waller, J. Karst, and G. von Freymann, *Light: Adv. Manuf.* **2**, 228 (2021).
- O. R. Opaluch, N. Oshnik, R. Nelz, and E. Neu, *Nanomaterials* **11**, 2108 (2021).
- D. D. Sukachev, A. Sipahigil, C. T. Nguyen, M. K. Bhaskar, R. E. Evans, F. Jelezko, and M. D. Lukin, *Phys. Rev. Lett.* **119**, 223602 (2017).
- Z.-H. Zhang, P. Stevenson, G. Thiering, B. C. Rose, D. Huang, A. M. Edmonds, M. L. Markham, S. A. Lyon, A. Gali, and N. P. de Leon, *Phys. Rev. Lett.* **125**, 237402 (2020).
- A. Gottscholl, M. Diez, V. Soltamov, C. Kasper, A. Sperlich, M. Kianinia, C. Bradac, I. Aharonovich, and V. Dyakonov, *Sci. Adv.* **7**, eabf3630 (2021).
- D. J. Christle, A. L. Falk, P. Andrich, P. V. Klimov, J. U. Hassan, N. T. Son, E. Jánzén, T. Ohshima, and D. D. Awschalom, *Nat. Mater.* **14**, 160 (2015).
- M. Langbecker, R. Wirtz, F. Knoch, M. Noaman, T. Speck, and P. Windpassinger, *New J. Phys.* **20**, 083038 (2018).
- E. Vetsch, D. Reitz, G. Sagué, R. Schmidt, S. T. Dawkins, and A. Rauschenbeutel, *Phys. Rev. Lett.* **104**, 203603 (2010).
- M. Vogel, R. Aßmann, P. Pirro, A. V. Chumak, B. Hillebrands, and G. von Freymann, *Sci. Rep.* **8**, 11099 (2018).
- E. H. Waller, S. Dix, J. Gutsche, A. Widera, and G. von Freymann, *Micromachines* **10**, 827 (2019).
- K. W. Kark, *Antennen und Strahlungsfelder*, 8th ed. (Springer Fachmedien Wiesbaden GmbH and Springer Vieweg, Wiesbaden, 2020).
- A. Dréau, M. Lesik, L. Rondin, P. Spinicelli, O. Arcizet, J.-F. Roch, and V. Jacques, *Phys. Rev. B* **84**, 195204 (2011).
- G. Mariani, S. Nomoto, S. Kashiwaya, and S. Nomura, *Sci. Rep.* **10**, 4813 (2020).
- K.-M. C. Fu, C. Santori, P. E. Barclay, L. J. Rogers, N. B. Manson, and R. G. Beausoleil, *Phys. Rev. Lett.* **103**, 256404 (2009).